

## Er-doped light emitting slot waveguides monolithically integrated in a silicon photonic chip

This article has been downloaded from IOPscience. Please scroll down to see the full text article.

2013 Nanotechnology 24 115202

(<http://iopscience.iop.org/0957-4484/24/11/115202>)

View [the table of contents for this issue](#), or go to the [journal homepage](#) for more

Download details:

IP Address: 158.109.36.236

The article was downloaded on 01/03/2013 at 09:41

Please note that [terms and conditions apply](#).

# Er-doped light emitting slot waveguides monolithically integrated in a silicon photonic chip

J M Ramírez<sup>1</sup>, F Ferrarese Lupi<sup>1</sup>, Y Berencén<sup>1</sup>, A Anopchenko<sup>2</sup>,  
J P Colonna<sup>3</sup>, O Jambois<sup>1</sup>, J M Fedeli<sup>3</sup>, L Pavese<sup>2</sup>, N Prtljaga<sup>2</sup>,  
P Rivallin<sup>3</sup>, A Tengattini<sup>2</sup>, D Navarro-Urrios<sup>4</sup> and B Garrido<sup>1</sup>

<sup>1</sup> MIND-IN2UB, Departament d'Electrònica, Universitat de Barcelona, Martí i Franquès 1, E-08028 Barcelona, Spain

<sup>2</sup> Nanoscience Laboratory, Department of Physics, University of Trento, Via Sommarive 14, Povo I-38123, Italy

<sup>3</sup> CEA, Léti, Minatec campus 17 rue des Martyrs, F-38054 Grenoble cedex 9, France

<sup>4</sup> Catalan Institute of Nanotechnology (CIN2-CSIC), Campus UAB, edifici CM3, E-08193 Bellaterra, Spain

E-mail: [jmramirez@el.ub.es](mailto:jmramirez@el.ub.es)

Received 3 July 2012, in final form 25 January 2013

Published 28 February 2013

Online at [stacks.iop.org/Nano/24/115202](http://stacks.iop.org/Nano/24/115202)

## Abstract

An integrated erbium-based light emitting diode has been realized in a waveguide configuration allowing 1.54  $\mu\text{m}$  light signal routing in silicon photonic circuits. This injection device is based on an asymmetric horizontal slot waveguide where the active slot material is  $\text{Er}^{3+}$  in  $\text{SiO}_2$  or  $\text{Er}^{3+}$  in Si-rich oxide. The active horizontal slot waveguide allows optical confinement, guiding and lateral extraction of the light for on-chip distribution. Light is then coupled through a taper section to a passive Si waveguide terminated by a grating which extracts (or inserts) the light signal for measuring purposes. We measured an optical power density in the range of tens of  $\mu\text{W}/\text{cm}^2$  which follows a super-linear dependence on injected current density. When the device is biased at high current density, upon a voltage pulse (pump signal), free-carrier and space charge absorption losses become large, attenuating a probe signal by more than 60 dB/cm and thus behaving conceptually as an electro-optical modulator. The integrated device reported here is the first example, still to be optimized, of a fundamental block to realize an integrated silicon photonic circuit with monolithic integration of the light emitter.

(Some figures may appear in colour only in the online journal)

## 1. Introduction

One of the open challenges in silicon photonics is a monolithically integrated light source [1]. Up to date, from the standalone device point of view, the most successful approach is based on heavily doped strained germanium on silicon. Indeed, an injection laser emitting around 1.5  $\mu\text{m}$  based on this material has been recently demonstrated [2]. However, the feasibility of its integration into silicon technology has yet to be demonstrated owing to the narrow process

margins in its fabrication. On the other hand, and as an alternative to high refractive index Ge, it is appealing to exploit silicon oxide since it has a very high refractive index contrast with silicon, is a good host for optically active rare earth ions (e.g.,  $\text{Er}^{3+}$ ) [3], and is a matrix where Si nanoclusters (Si-ncs) can be easily formed (then obtaining the silicon-rich oxide, SRO). The last point is instrumental for optically pumped devices which increase and spectrally broaden the effective  $\text{Er}^{3+}$  excitation cross-section through the Si-ncs sensitization process [4, 5]. For electrically pumped

devices SRO is also beneficial as a controlled injector. The gate electrode/SRO energy band offset can be easily adjusted depending on the silicon excess precipitation (the higher the silicon excess precipitation of the SRO, the lower the energy barrier). Furthermore, the density of silicon precipitates and related defects modulate the conductivity of the SRO (and thus the average energy distribution of the conducting electrons), which in turn translates into an Er impact ionization efficiency [6–8]. Moreover, an enhancement of the  $\text{Er}^{3+}$  emission in doped Si-ncs is expected due to the Purcell effect [9, 10].  $\text{Er}^{3+}$ -doped active waveguides are easy to fabricate by using the concept of a slot waveguide [11], where optical confinement inside a thin slot layer of low refractive index material is achieved. Low propagation losses can be achieved even in slot waveguide structures designed for electrical injection [12]. Thus silicon slot waveguides provide a MOS (metal–oxide–semiconductor) capacitor type of injecting structure while at the same time maintaining light confinement and propagation along the slot. This makes possible lateral light extraction for on-chip distribution, in contrast with standard MOSLED (metal–oxide–semiconductor light emitting diode), where light emission is vertical [13, 14].

In this work we demonstrate a light emitting diode working at  $1.54 \mu\text{m}$  integrated within a slot waveguide and coupled to a passive waveguide through a tapered region. The light emission can be directly modulated by the electrode voltage signal and distributed on-chip. Although yet to be demonstrated, should the slot material have net gain due to  $\text{Er}^{3+}$  inversion, optical feedback in the slot waveguide section through a Fabry–Perot or a micro-ring resonator would allow laser emission at  $1.54 \mu\text{m}$  in an integrated functional configuration.

## 2. Device performance

Figure 1 shows the realized device, where an active waveguide is coupled to a passive waveguide that ends in a surface grating for light signal extraction. The devices were fabricated in a CMOS (complementary MOS) line on a p-type silicon on insulator (SOI) wafer with a 220 nm thick silicon device layer and 2  $\mu\text{m}$  buried oxide (BOX). The active waveguide geometry is based on an asymmetric slot waveguide, where a thin 40 nm slot layer is sandwiched between two silicon-doped layers to permit electrical injection in the slot. The waveguide width is 1  $\mu\text{m}$ . The design has been optimized by using a fully vectorial mode solver based on the film mode matching (FMM) method. Optimization yields an asymmetric geometry to enhance the optical confinement of the transverse magnetic (TM) polarized mode in the slot region. In this way, the mode overlap with the top polysilicon electrode is minimized, which, in turn, decreases the absorption losses. The bottom electrode of the waveguide has been produced by means of a boron implantation with a dose of  $5 \times 10^{12} \text{ at. cm}^{-2}$  at 25 keV of energy. Two different materials have been used in the slot layer:  $\text{Er}^{3+}$ -doped  $\text{SiO}_2$  (high temperature oxide) and  $\text{Er}^{3+}$ -doped SRO. The SRO has been deposited by low-pressure chemical vapour deposition (LPCVD) with a

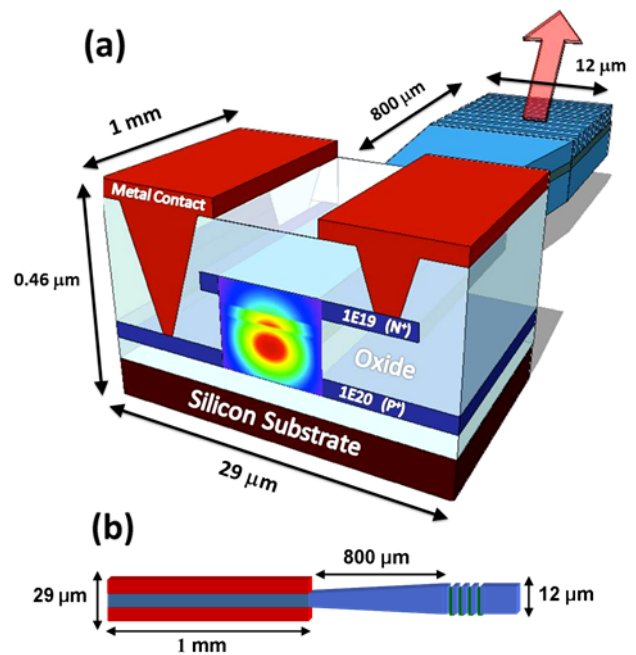


**Figure 1.** (a) 3D schematics of the integrated photonic device. On the cross-section of the active slot waveguide (40 nm of slot) we have reported the simulated profile of the fundamental TM mode. The blue region refers to silicon, light blue to silicon oxide and red to metals. (b) Top view of the integrated system with the active slot waveguide (left), the slot taper (centre) and the passive Si waveguide with the output coupler (right).

silicon excess of 11.5%, then annealed at  $900^\circ\text{C}$  for 1 h in a  $\text{N}_2$  atmosphere in order to promote the phase separation and nanocluster precipitation (step I in figure 2).  $\text{Er}^{3+}$  doping was obtained by ion implantation to get an Er concentration peak of  $5 \times 10^{20} \text{ at. cm}^{-3}$ . For the sake of clarity, the waveguide containing the  $\text{Er}^{3+}$  and Si-ncs will be labelled as Er:Si-ncs, while the other one is labelled as Er: $\text{SiO}_2$ . Subsequently, undoped polysilicon 100 nm thick and high-temperature oxide 180 nm thick were deposited on top of the layers (figure 2, step II). The lower slab in the waveguide (Si pedestal) and the bottom electrode wings were then formed through partial silicon etch at the sides of the waveguide structure, starting from the top polysilicon, the active layer and finally the bottom polysilicon down to 90 nm (thickness of the bottom electrode).

The 220 nm thick Si pedestal has graded p-type doping in order to reduce the free-carrier density in the optical mode region. The gradient in the doping was achieved by several boron implantations which yielded a doping of  $\sim 10^{17} \text{ at. cm}^{-3}$  in the region under the active slot layer. This value gradually increases to  $\sim 10^{19} \text{ at. cm}^{-3}$  in the region far from the active slot layer and becomes  $\sim 10^{20} \text{ at. cm}^{-3}$  in the 90 nm thick bottom electrode. Notice that this step becomes crucial for proper device operation. For this purpose the implantation dose and energy values were first simulated in order to adjust a proper lateral diffusion (in the  $x$  direction) of the implanted ions, taking advantage of the isotropic condition in the monocrystalline silicon (figure 2, step III). A cross-section view of the simulated boron concentration and

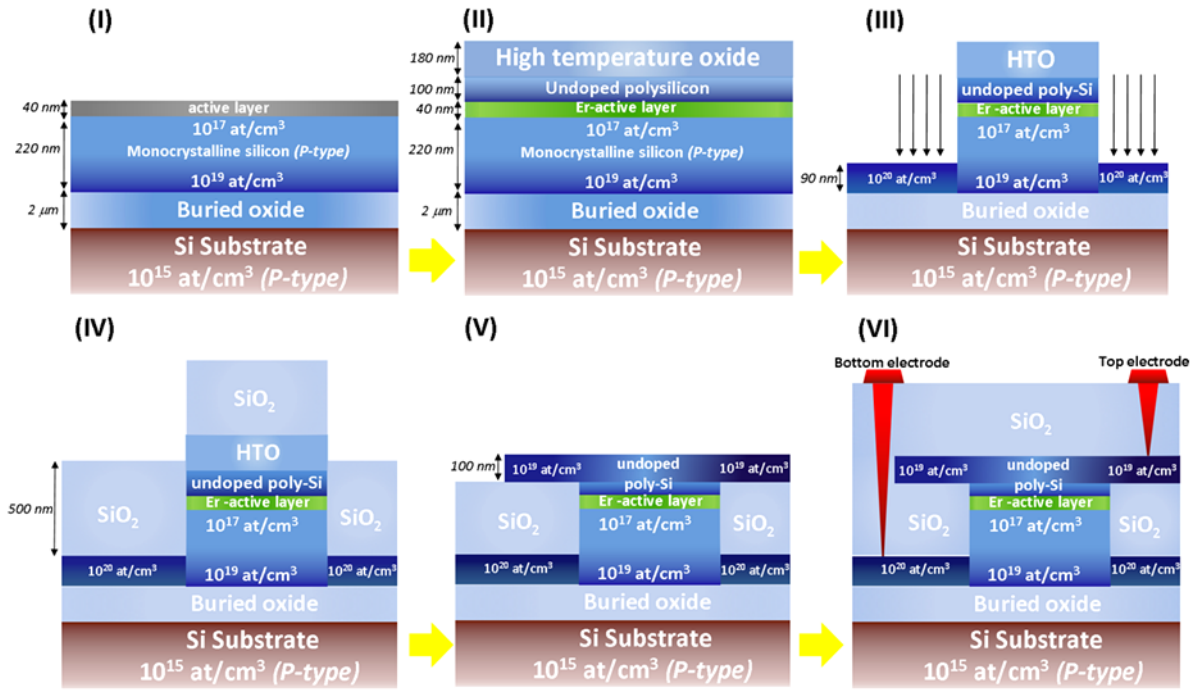


Figure 2. Process flow of the slot waveguides.

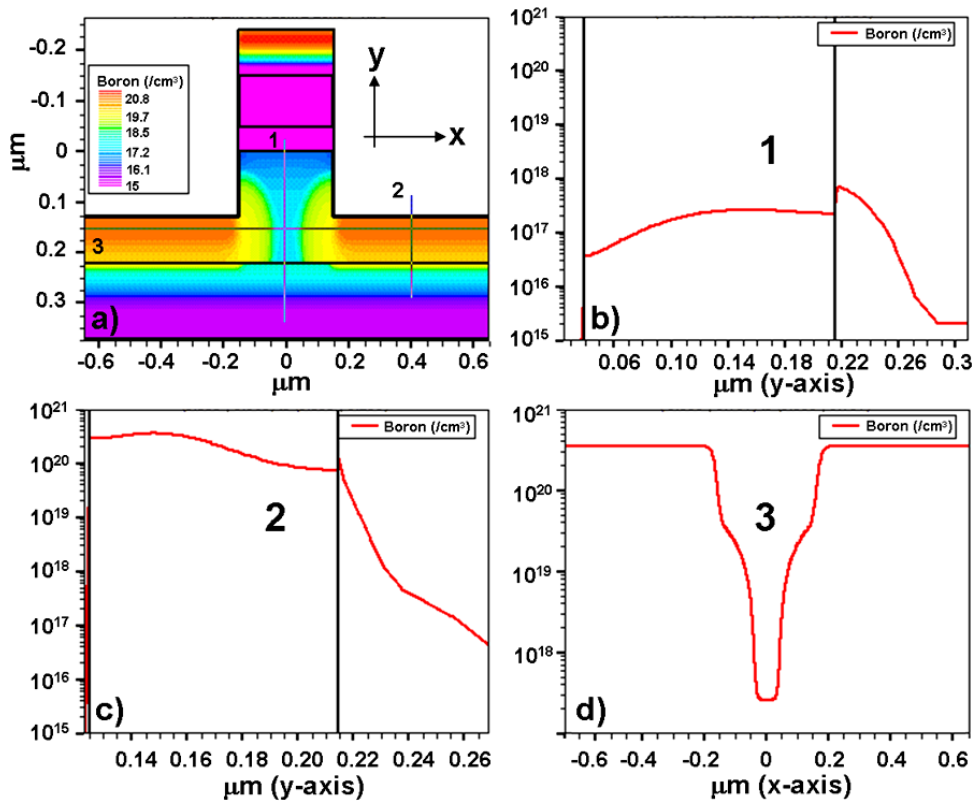


Figure 3. (a) Total boron concentration inside the waveguide. A coloured legend and a coordinate system ( $x$ - $y$ ) with labelled straight lines (1, 2 and 3) have been defined to show the doping gradient (at.  $\text{cm}^{-3}$ ) and the concentration profile in three different sections, i.e. the Si pedestal (b, line 1), the bottom electrode wing (c, line 2) and along the bottom electrode cross-section (d, line 3).

three different profiles (two in the  $y$  axis and one across the  $x$  axis) are shown in figure 3 to illustrate the doping. Profile 1 (figure 3(b)) accounts for the graded doping in the Si pedestal

(lower asymmetric slab), with a minimum (maximum) boron concentration of  $3 \times 10^{16}$  at.  $\text{cm}^{-3}$  ( $10^{18}$  at.  $\text{cm}^{-3}$ ). It is worth noticing that the top doping values were defined lower than

the ones reported for the final device because of the expected lateral diffusion (in the  $x$  direction) of electrode dopants when submitted to the thermal treatment, hence increasing the total doping in the Si pedestal. Profiles 2 and 3 (figures 3(c) and (d)) show the boron doping concentration for the bottom electrode wing in the  $y$  axis and  $x$  axis directions, respectively (a maximum of  $3.5 \times 10^{20}$  at.  $\text{cm}^{-3}$  is expected in both cases). Then,  $\text{Er}^{3+}$  activation and matrix damage recovery were performed on both layers through a post-annealing treatment at  $800^\circ\text{C}$  for 6 h.

Afterwards, a 500 nm thick  $\text{SiO}_2$  was deposited on the top polysilicon and used as a spacer (figure 2, step IV), followed by a chemical polishing of the surface, reducing the upper polysilicon thickness from 100 nm down to 20 nm. The 100 nm thick top silicon layer is formed by polycrystalline silicon deposition at  $620^\circ\text{C}$  without intentional doping. Only the side regions (wings) are doped by a phosphorus implantation, obtaining a maximum doping concentration of  $\sim 10^{19}$  at.  $\text{cm}^{-3}$  (figure 2, step V). The dopants of both electrodes were activated by a fast annealing at  $950^\circ\text{C}$  for 60 s. The highly doped electrodes are finally contacted by the metallization, for which TiN and AlCu alloys have been used (figure 2, step VI). It is worth noticing that the top polysilicon layer is almost transparent for the vertically emitted photons at  $1.54 \mu\text{m}$  by  $\text{Er}^{3+}$  ions. The final active device size is: 1 mm (length)  $\times$   $29 \mu\text{m}$  (width)  $\times$   $0.46 \mu\text{m}$  (height). Passive propagation losses in these devices at  $1.54 \mu\text{m}$  were  $\sim 4$  dB, which is high but commensurate with the length of the slot section (1 mm). A passive slot waveguide-based taper was also fabricated to optimize the coupling between the active device and the passive waveguide. The taper tip is  $1 \mu\text{m}$  wide at the beginning (equal to the active section) and it extends for  $800 \mu\text{m}$  with a final width of  $12 \mu\text{m}$  matching the width of passive section. The same steps were used in the process flow for the taper and passive waveguide fabrication, except for the doping and the  $\text{Er}^{3+}$  implantation. Finally, the light extraction was carried out through an output coupler. The grating coupler was fabricated after the taper-passive waveguide system, by engraving trenches in the passive waveguide down to the monocrystalline silicon. Such a structure is  $16 \mu\text{m}$  long and  $12 \mu\text{m}$  wide, with a grating period of  $0.8 \mu\text{m}$ , a grating groove depth of 150 nm and a collection angle tilted  $25^\circ$  from the normal. Notice that the passive device geometry (slot taper and output coupler) was designed in accordance with the technological constraints (i.e. they were adjusted to ease alignment tolerances).

The electric polarization of the active waveguides was performed using a semiconductor device analyser (Agilent B1500 equipped with high-resolution measurement units) and a Cascade Microtech SUMMIT probe station with Faraday and optical shielding, atguard and triaxial cabling, adapted in order to perform both optical and electrical characterization. The emitted light was collected with an infrared objective and then coupled to a grating spectrometer interfaced with a calibrated photomultiplier. Placing the objective on top of the active waveguide allows recording of the scattered light fraction emitted vertically by the waveguide, while placing the objective on the grating

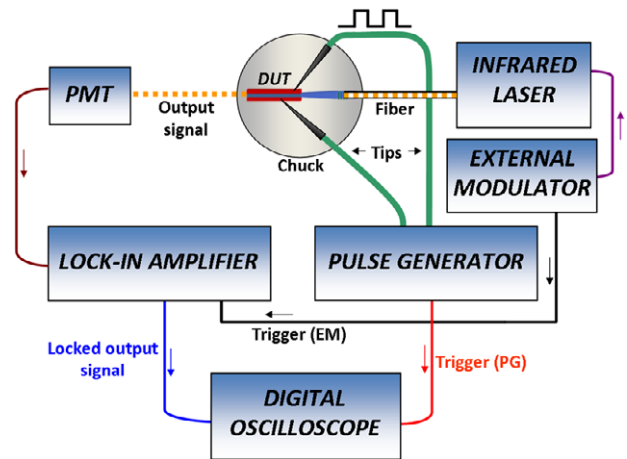
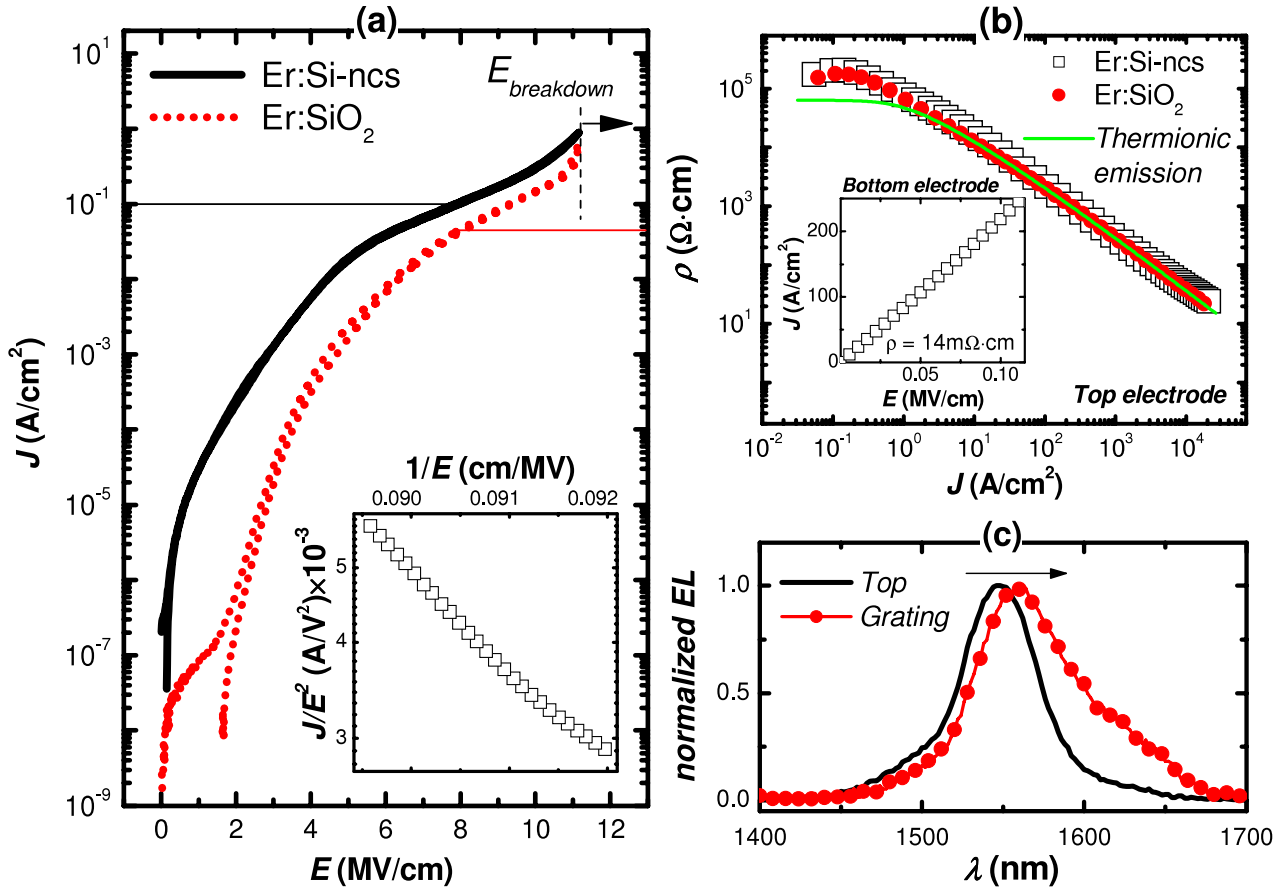


Figure 4. Electrical pump and probe setup.

allows measurement of the guided light fraction along the waveguide. This guided light is then channelled into the passive waveguide and out-coupled through the grating. By using the grating as an input port and a cleaved facet of the active waveguide as the output port, it is possible to perform transmission experiments (pump and probe measurements) where electrical excitation of the waveguide acts as a pump signal, the probe signal being provided by an external laser coupled into the waveguide (see figure 4). For this purpose the waveguide was driven with a pulse generator (square pulsed voltage at 10 Hz) while the probe signal was provided by an infrared laser at 1528 nm, externally modulated at 200 kHz using an arbitrary waveform generator. The transmitted signal was measured by using a lock-in amplifier synchronized with the probe to filter out the electroluminescence (EL). Finally the signals were monitored with a digital oscilloscope with a temporal resolution of  $0.5 \mu\text{s}$ .

### 3. Results and discussion

Figure 5(a) shows the  $I(V)$  characteristics under forward bias of the active slot waveguides for the two slot materials studied ( $\text{Er}^{3+}$  in  $\text{SiO}_2$  and  $\text{Er}^{3+}$  in SRO). Forward bias means here that a DC negative voltage was applied to the n-type doped top electrode. This particular configuration yields electron injection at the top electrode and hole accumulation at the lower interface. We will not give details on inversion (reverse bias) characteristics here as the currents involved are orders of magnitude lower (rectification) and thus light emission is very poor. As demonstrated in earlier test capacitors of a similar type driven into accumulation [8, 15], hole transport through the slot can be ruled out due to the large energy offsets between the valence bands of silicon and those of  $\text{SiO}_2$  or SRO, which are in the range 4.0–4.7 eV. Instead, the band offset for electrons is in the range 1.6–3.1 eV (depending on silicon excess precipitation). Nevertheless, one expects a certain degree of hole injection and trapping at the lower interface (seen as displacement current), as previously demonstrated in pulse programming of Si-ncs memories [16]. The devices were biased up to device



**Figure 5.** (a) Current density versus applied electric field  $J(E)$  characteristics for the Er:Si-ncs device (solid line) and the Er:SiO<sub>2</sub> device (dotted line) up to device breakdown. Horizontal lines mark the onset of electroluminescence for the two devices. Inset, the Fowler–Nordheim plot for the Er:SiO<sub>2</sub> device. (b) Resistivity values of the top electrode for the Er:Si-ncs device (empty squares) and the Er:SiO<sub>2</sub> device (filled dots) as a function of the injected current density. The line shows the curve fitting using the thermionic emission model. Inset,  $J(E)$  characteristic for the bottom electrode. (c) Comparison between the emitted EL spectrum collected from the active waveguide surface (straight line) and from the output grating coupler (dotted line).

breakdown, which was usually between 11 and 12 MV cm<sup>-1</sup>, a value that is compatible with a high-quality silica layer grown on silicon [17]. The voltage sweeping step was fixed at 50 mV s<sup>-1</sup>, which is small enough for achieving quasi-static  $I(V)$  curves by allowing trap charging/discharging quasi-equilibrium at each step (as seen from the pulsed polarization dynamics of the system). The horizontal lines in figure 5(a) represent the current density threshold for EL emission (red for the Er:SiO<sub>2</sub> device and black for the Er:Si-ncs device). Specifically, the threshold field for light emission was around 6.5 MV cm<sup>-1</sup> for both samples and threshold currents were 64 mA cm<sup>-2</sup> and 26 mA cm<sup>-2</sup> for the Er:Si-ncs and the Er:SiO<sub>2</sub> devices, respectively. These values of threshold field correlate with the onset for the electrode-limited Fowler–Nordheim tunnelling current, which starts to dominate at around 6 MV cm<sup>-1</sup>. We can consider this threshold as a profound modification of the transport properties of electrons through the layer: (i) for voltages below this threshold, the current is bulk limited and proceeds by hopping between trap states (either tunnel or Poole–Frenkel type, as deduced from fittings not shown) for which carriers remain cold and do not gain enough energy

to excite Er<sup>3+</sup> ions and (ii) for voltages above this threshold, the electrons are injected into the conduction band of SiO<sub>2</sub> or SRO and are accelerated by the strong electric field up to average final energies in the range 3.0–4.5 eV for fields in the range 6–11 MV cm<sup>-1</sup>, as shown by DiMaria *et al* from Monte Carlo simulations [17]. Accelerated electrons thus have enough energy to impact and excite Er<sup>3+</sup> ions to the first excited (0.8 eV–1550 nm) or even to upper excited levels (1.27 eV–980 nm, 1.46 eV–850 nm, ...). The EL spectroscopy of the upper levels of Er<sup>3+</sup> (up to 2.54 eV–488 nm emission) can be observed in the emission spectra of MOSLED capacitors of similar type to the waveguides reported here [18]. As stated before, above the EL threshold, the  $I(V)$  characteristics are well within the Fowler–Nordheim tunnelling dependence (see inset of figure 4(a)). Thus, for a given electric field  $E$ , the tunnelling current density  $J$  through the active layers is [8, 19]:

$$J = \frac{q^3 E^2}{8\pi h \phi_b} \exp\left(-\frac{4\sqrt{2m_{\text{ox}}^*}(\phi_b)^3}{3\hbar q E}\right) \quad (1)$$

where  $q$  is the elementary charge,  $\hbar$  is the reduced Planck's constant,  $\phi_b$  is the potential barrier height at the electrode-active layer interface and  $m_{\text{ox}}^* = 0.5 m_e$  is the effective mass of the injected electrons [20, 21]. The curve fitting yields an effective barrier height of  $1.9 \pm 0.4$  eV ( $1.1 \pm 0.3$  eV) for the Er:SiO<sub>2</sub> (Er:Si-ncs) layer. These values are considerably lower than the ones reported in [8] for Er:SiO<sub>2</sub> (Er:Si-ncs) MOSLEDs, which we believe it is due to the presence of the lightly doped top polysilicon in the slot waveguide region, as we will demonstrate in the following. The injected current in the active layer is in fact preceded by the conduction mechanisms taking place within the lightly doped (high resistivity) upper polysilicon layer. These mechanisms were further validated by measuring additional test devices, where two metal stripes were contacted to the two side-wings of the top electrode. Results showed a current density dependent resistivity—from  $10^5 \Omega \cdot \text{cm}$  (at  $1 \text{ MV cm}^{-1}$ ) to  $15 \Omega \cdot \text{cm}$  (at  $11.5 \text{ MV cm}^{-1}$ ), as seen in figure 5(b). Therefore the dominant conduction mechanism through the lightly doped polysilicon is thermionic emission over the potential barriers at the grain boundaries (grain boundary carrier trapping mechanism) [22]. In this case, the expression for the current density ( $J$ ) is:

$$J = 2A^*T^2 \exp\left(\frac{q\phi_b}{kT}\right) \sinh\left(\frac{qV}{2kT} \cdot \frac{\langle a \rangle}{L}\right) \quad (2)$$

where  $A^*$  is Richardson's constant,  $\phi_b$  is the potential barrier height at the grain boundary,  $kT$  is the thermal energy,  $L$  is the length of the polysilicon layer,  $\langle a \rangle$  is the mean grain size and  $V$  the total applied voltage. From this equation, the resistivity can be obtained as:

$$\rho = \frac{V}{LJ} = \frac{V}{2A^*LT^2} \frac{\exp\left(\frac{q\phi_b}{kT}\right)}{\sinh\left(\frac{qV}{2kT} \cdot \frac{\langle a \rangle}{L}\right)}. \quad (3)$$

A good fit to the data is obtained with a potential barrier height of  $0.43 \pm 0.05$  eV and a mean grain size of  $15 \pm 2$  nm (green line in figure 5(b)). Note that these values agree with previous reports on similar material [23, 24]. In contrast, the bottom electrode showed an Ohmic behaviour (see inset of figure 5(b)) with a resistivity of  $14 \text{ m}\Omega \cdot \text{cm}$ . As a result, the low barrier height  $\phi_b$  found at the electrode-active layer interface can be explained by assuming that injected electrons already face the electrode-active layer interface with energies above the conduction band (warm electrons) as a consequence of the thermionic transport and acceleration due to the voltage drop within the lightly doped polysilicon electrode [25].

Figure 5(c) shows the normalized Er<sup>3+</sup> spectra collected either at the active waveguide surface (straight line) or at the output grating coupler (dotted line) for a bias of  $10 \text{ MV cm}^{-1}$ . The typical Er<sup>3+</sup> emission spectrum is observed. Er<sup>3+</sup> are excited mainly by impact excitation of highly energetic carriers after acceleration in the SiO<sub>2</sub> or SRO [8]. Note a shift of about 10 nm and a different line shape between the two spectra. Since this shift and line shape difference are not observed when EL is collected from a cleaved facet of the active waveguide, they are thought to be due to the filtering action of the output grating due to some unavoidable random errors in its fabrication [26].

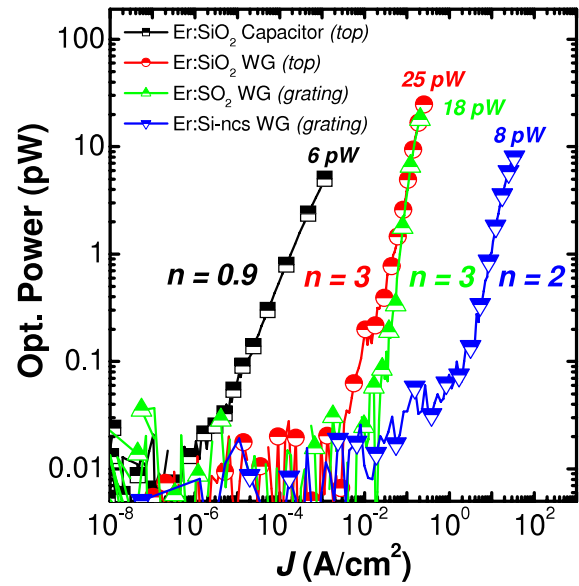


**Figure 6.** Optical power as a function of the injected current density for both waveguide devices (circles correspond to vertical EL collected from the waveguide of the Er:SiO<sub>2</sub> device, while the triangles correspond to the EL recorded from the grating either of the Er:SiO<sub>2</sub> or of the Er:Si-ncs devices) and for an Er<sup>3+</sup>-doped SiO<sub>2</sub> capacitor (squares) used as a control device. The devices were biased from 0 V to  $-46$  V (close to voltage breakdown). Let us note that to facilitate the comparison the emitted optical power of the capacitor has been scaled by 10 to reduce its effective area to the active waveguide area ( $10^{-5} \text{ cm}^2$ ). This scaling is based on the linear relation we found between the emitted optical power and the area of similar MOS devices.

Figure 6 reports the emitted optical power versus the injected current density for the two devices studied here as well as for a capacitor MOSLED control device used as reference. The control device consists of a highly n-type doped ( $10^{20} \text{ at. cm}^{-3}$ ) top polysilicon gate electrode (100 nm thick) with a surface of  $10^{-4} \text{ cm}^2$ , a 40 nm thick Er<sup>3+</sup>-doped SiO<sub>2</sub> active layer with the same characteristic as the slot layer in the Er:SiO<sub>2</sub> device, and a bottom p-type Si substrate [8]. As can be observed in figure 6, the control device (capacitor) has the lowest EL threshold current density ( $5 \times 10^{-6} \text{ A cm}^{-2}$ ). This value is four orders of magnitude lower than those for the waveguide devices ( $\sim 10^{-2} \text{ A cm}^{-2}$ ). On the other hand, the emitted optical powers are of the same order of magnitude (but slightly higher for the slot waveguides). This fact suggests a lower external quantum efficiency ( $\eta_{\text{ext}}$ ) for the waveguide devices than for the control capacitor. The low  $\eta_{\text{ext}}$  may be due to a low extraction efficiency and/or a low internal quantum efficiency ( $\eta_{\text{int}}$ ). A low  $\eta_{\text{int}}$  might be due to the resistive polysilicon injectors, where a significant voltage drop occurs, which in turn decreases the electric field strength for impact excitation of Er<sup>3+</sup> ions. In addition, the maximum emitted power collected at the waveguide surface (half-filled circles in figure 6) and at the grating (half-filled triangles in figure 6) are similar. This suggests that a good coupling efficiency between the active and the passive waveguide is achieved and that most of the coupled light exits from the grating. The Er:Si-ncs waveguide device has lower  $\eta_{\text{ext}}$  than the Er:SiO<sub>2</sub> waveguide device (see the

inverted half-filled triangles in figure 6). This is expected since the electron energy distribution is anticipated to be colder for SRO than for SiO<sub>2</sub>. Si-ncs act as trapping centres (and thus as pathways for cold electron hopping conduction) but also as scattering centres for energetic electrons in the conduction band. Additional reasons rely on the fact that a significant fraction of Er<sup>3+</sup> in Si-ncs can be non-radiative due to additional defects in the material or an insufficient oxidation state of Er due to the presence of Si–Si bonds [27]. Remarkably, the light emission (EL) versus current density ( $J$ ) characteristics shows a power law dependence with an ‘ $n$ ’ exponent:

$$EL \propto J^n \quad (4)$$

with  $n = 0.9$  for the capacitor [15],  $n = 2$  for the Er:Si-ncs device and  $n = 3$  for the Er:SiO<sub>2</sub> device. The super-linear  $EL(J)$  dependence of the emission in the waveguides was further validated by measuring many other devices with 2 and 3 mm long active waveguides in the photonic chip, finding no correlation between the super-linear behaviour (higher ‘ $n$ ’ exponents) and the waveguide length. Additional experiments on the lifetime of Er<sup>3+</sup> emission show that the lifetime drops for high voltage and high current injection. Nevertheless, we discard stimulated emission to explaining super-linearity since we did not observe any line narrowing in the emission spectra when  $J$  is increased. Furthermore, the super-linearity can also be observed in the  $EL(J)$  collected at the waveguide surface (vertical emission) were the cavity amplification effect is completely ruled out (data reported as half-filled circles for the Er:SiO<sub>2</sub> waveguide in figure 6). To suggest an explanation of the origin of the super-linearity we note that the main electrical difference between the capacitor and the waveguide devices is the electrical characteristic of the top electrode. In the capacitor it behaves as Ohmic contact (resistivity of 4 mΩ · cm) while in the waveguide devices it is a thermionic injector. Therefore, it is reasonable to assume that the upper electrode is not equipotential in all of its area. For low  $J$ , most of the electron injection occurs near the wings of the silicon top electrode due to the high polysilicon resistivity. At high  $J$ , i.e. high electric fields, the injection spreads over the whole active layer since the polysilicon resistivity drops. This increases the effective excited active layer volume, which explains the  $EL(J)$  nonlinearity. As an alternative explanation, one may adopt that the most energetic hot electrons can excite multiple Er<sup>3+</sup> ions, but, again, if this was the case, super-linearity should also be observed for capacitors. Since the effective barrier height is larger for Er:SiO<sub>2</sub> than for Er:Si-ncs, we expect the EL to grow faster for the former.

Finally, in order to evaluate the additional absorption losses of the waveguides due to injected carriers, we performed transmission measurements of a probe laser signal at 1.54 μm with electrical pumping of the waveguide (electrical pump and optical probe configuration). The inset (a) of figure 7 shows that the transmitted spectrum of the probe signal attenuates significantly when the bias is switched on. The analysis of the time dependence of the probe transmitted signal (inset (b) of figure 7) revealed a time response of few microseconds, which can be directly related to the free-carrier

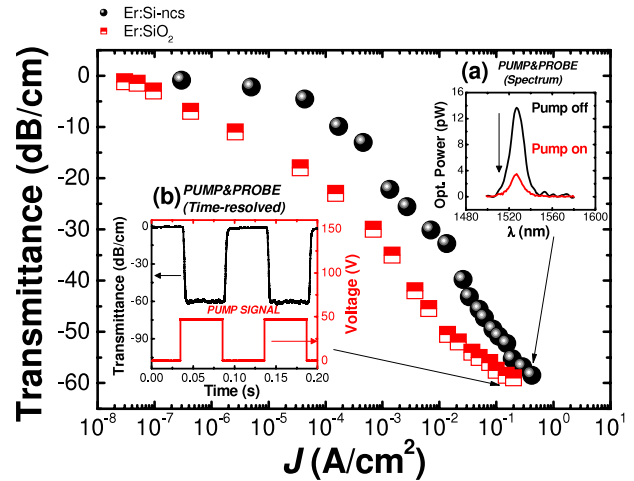


**Figure 7.** Free-carrier absorption (in dB cm<sup>-1</sup>) of the waveguide device at 1528 nm as a function of the injected current density  $J$ . Inset (a), the attenuation of the probe spectrum when the bias is switched on. Inset (b), the modulated voltage and the transmitted signal as a function of time for the highest current density used.

lifetime. The probe transmittance decreases significantly when the injected current density is increased (figure 7). Consequently, we conclude that additional absorption at high current is due to carrier absorption, either trapped carriers (which generate space charge in the SiO<sub>2</sub> and SRO) or free conducting carriers. A maximum probe transmittance attenuation of -60 dB cm<sup>-1</sup> (at 0.5 A cm<sup>-2</sup>) is observed for both waveguide devices. Note that the Er:SiO<sub>2</sub> device shows higher carrier absorption than the Er:Si-ncs device. This difference can be explained by the fact that the sample containing Si-ncs is more conductive and space charge is expected to be less prominent. To further corroborate this hypothesis, notice that current–voltage characteristics reveal a wider shift between progressive and regressive  $I$ – $V$  scans for the Er:SiO<sub>2</sub> device than for the Er:Si-ncs device (see figure 5(a) at low applied bias). This hysteresis width is directly related to the trapped charge density. This behaviour can be translated directly into an electro-optical modulator concept with a 60 dB cm<sup>-1</sup> of attenuation difference of the probe beam between ‘on’ and ‘off’ states. This electro-optical modulator could then be engineered together with the light emitting source. In these non-optimized devices, the measured carrier absorption time response was in the range of few μs (equal to our setup resolution) suggesting device operation frequencies of at least hundreds of kHz.

#### 4. Conclusions

In summary, Er<sup>3+</sup>-doped Si-based light emitting slot waveguides were designed, fabricated and characterized. Two different compositions of the active layer were compared: an Er<sup>3+</sup>-doped SiO<sub>2</sub> layer and an Er<sup>3+</sup> and Si-ncs codoped SiO<sub>2</sub> layer. It was demonstrated that Si-ncs are useful to get a better injection into the active device layer. On the other hand, the Er<sup>3+</sup>-doped silica active layer yields higher efficiency since more hot carriers can be injected in an active material, leading to more efficient Er<sup>3+</sup> impact excitation.

It is worth noting that the waveguide device ensures the propagation of emitted radiation. This allows an interface with a similar passive waveguide and emitted signal collection through a surface grating structure. This is also a first example of a monolithically integrated infrared source that can be used in silicon photonics. Moreover, this work clarifies the route towards further device optimization. In fact, most of the limitations are associated with the device electrodes. In addition, a novel use of the free-carrier absorption which results from the injection of free carriers into slot waveguides is suggested: an integrated modulator with a high extinction ratio or an integrated variable-optical attenuator. Finally, here is reported a first attempt at a monolithic integrated optoelectronic chip where the source, the waveguide and the output couplers are simultaneously fabricated within the same CMOS compatible process.

## Acknowledgments

This work was supported by the Spanish Ministry of Science through the project LASSI (TEC2009-08359), by the EC through the project ICT-FP7-224312 HELIOS and by Italy–Spain integrated actions. D N-U is grateful for the financial support of AGAUR through the Beatriu de Pinòs program.

## References

- [1] Pavesi L, Dal Negro L, Mazzoleni C, Franzò G and Priolo F 2000 *Nature* **408** 440–4
- [2] Camacho-Aguilera R E, Cai Y, Patel N, Bessette J T, Romagnoli M, Kimerling L C and Michel J 2012 *Opt. Express* **20** 11316–20
- [3] Adler D L, Jacobson D C, Eaglesham D J, Marcus M A, Benton J L, Poate J M and Citrin P H 1992 *Appl. Phys. Lett.* **61** 2181–3
- [4] Fuji M, Yoshida M, Kanzawa Y, Hayashi S and Yamamoto K 1997 *Appl. Phys. Lett.* **71** 1198–200
- [5] Izzedin I, Timmerman D, Gregorkiewicz T, Moskalenko A S, Prokofiev A A, Yassievich N and Fujii M 2008 *Phys. Rev. B* **78** 035327
- [6] DiMaria D J and Dong D W 1980 *J. Appl. Phys.* **51** 2722–35
- [7] Jambois O *et al* 2012 *J. Phys. D: Appl. Phys.* **45** 045103
- [8] Ramírez J M *et al* 2012 *Nanotechnology* **23** 125203
- [9] Jayatilaka H, Nasrollahy-Shiraz A and Kenyon A J 2011 *Opt. Express* **19** 24569–76
- [10] Creatore C, Andreani L C, Miritello M, Lo Savio R and Priolo F 2009 *Appl. Phys. Lett.* **94** 103112
- [11] Almeida V R, Xu Q, Barrios C A and Lipson M 2004 *Opt. Lett.* **29** 1209–11
- [12] Preston K and Lipson M 2009 *Opt. Express* **17** 1527–34
- [13] Walters R J, Bourianoff G I and Atwater H A 2005 *Nature Mater.* **4** 143–6
- [14] Sun J M, Skorupa W, Dekorsky T, Helm M, Rebohle L and Gebel T 2005 *J. Appl. Phys.* **97** 123513
- [15] Anopchenko A *et al* 2012 *J. Appl. Phys.* **111** 063102
- [16] Garrido B, Cheylan S, González-Varona O, Pérez-Rodríguez A and Morante J R 2003 *Appl. Phys. Lett.* **82** 4818–20
- [17] Arnold D, Cartier E and DiMaria D J 1994 *Phys. Rev. B* **49** 10278
- [18] Ramírez J M *et al* 2012 *Mater. Sci. Eng. B* **177** 734
- [19] Fowler R H and Nordheim L 1928 *Proc. R. Soc. A* **119** 181
- [20] Hadjadj A, Simonetti O, Maurel T, Salace G and Petit C 2002 *Appl. Phys. Lett.* **80** 3335
- [21] DiMaria D J, Kirtley J R, Pakulis E J, Dong D W, Kuan T S, Pesavento F L, Theis T N and Cutro J A 1984 *J. Appl. Phys.* **56** 401
- [22] Lee J Y M and Cheng C 1982 *J. Appl. Phys.* **53** 490
- [23] Joshi D P and Bhatt D P 1990 *IEEE Trans. Electron Devices.* **37** 237
- [24] Säynätjoki A, Riikonen J and Lipsanen H J 2003 *Mater. Sci.: Mater. Electron.* **14** 417
- [25] Umemoto Y, Schaff W J, Park H and Eastman L F 1993 *Appl. Phys. Lett.* **62** 1964
- [26] Roelkens G, Van Thourhout D and Baets R 2006 *Opt. Express* **14** 11622–30
- [27] Priolo F, Presti C D, Franzò G, Irrera A, Crupi I, Iacona F, Di Stefano G, Piana A, Sanfilippo D and Fallica P G 2006 *Phys. Rev. B* **73** 113302